Article:
Mumtaz, Asim, Ma, Kyung Yeol, Shalvey, Thomas et al. (2026) Incorporation of 2-D hexagonal boron nitride in thin film solar cells. 2d Materials. 035012. ISSN: 2053-1583

https://doi.org/10.1088/2053-1583/ae8033

Incorporation of 2-D hexagonal boron nitride in thin film solar cells

2D Materials

PAPER

OPEN ACCESS

RECEIVED
26 November 2025

REVISED
14 May 2026

ACCEPTED FOR PUBLICATION
22 June 2026

PUBLISHED
3 July 2026

Incorporation of 2-D hexagonal boron nitride in thin film solar cells

Asim Mumtaz[1,2,*], **Kyung Yeol Ma**[3,4], **Thomas Shalvey**[2], **Luke Thomas**[2], **Maha Alotaibi**[5,1], **Gonzalo Vallejo Fernandez**[1], **Andrew Pratt**[1], **Jonathan D Major**[2], **Hyeon Suk Shin**[4,6] and **Ken Durose**[2]

[1] School of Physics, Engineering & Technology, University of York, Heslington, York YO10 5DD, United Kingdom
[2] Department of Physics, Stephenson Institute for Renewable Energy, University of Liverpool, Liverpool L69 7ZF, United Kingdom
[3] Research Laboratory of Electronics, Massachusetts Institute of Technology, Cambridge, MA 02139, United States of America
[4] Center for 2D Quantum heterostructures, Institute for Basic Science (IBS), Suwon 16419, Republic of Korea
[5] Department of Physics, College of Khurma University College, Taif University, PO Box 11099, Taif 21944, Saudi Arabia
[6] Department of Chemistry & Department of Energy, Sungkyunkwan University (SKKU), Suwon 16419, Republic of Korea
[*] Author to whom any correspondence should be addressed.

E-mail: asim.mumtaz@york.ac.uk

Keywords: two-dimensional hexagonal boron nitride, cadmium telluride, antimony selenide, solar cells, back contact

Supplementary material for this article is available online

Abstract

Owing to the properties of hexagonal boron nitride (hBN) such as its mechanical strength, high chemical and thermal stability, there has been significant interest in this two-dimensional material. This coupled with improved methods of synthesis has resulted in new applications. In this work we incorporate hexagonal boron nitride into thin film solar cells based on cadmium telluride and antimony selenide. This work entailed the deposition of a few layers of hexagonal boron nitride on the back surface of solar cells, sandwiched between the absorber layers (cadmium telluride, antimony selenide) and the metal contact. This study was designed to investigate whether hexagonal boron nitride would act to reduce the recombination rate in that region of the device. The consequence of this would be to enhance the open circuit voltage of the solar cells, which has been a blocking point for efficiency improvements in such solar cells. This study demonstrated improvements in performance of cadmium telluride solar cells. Therefore, this work opens new applications for hexagonal boron nitride in thin-film solar cells.

1. Introduction

2-dimensional (2D) hexagonal boron nitride (hBN) has received much interest in recent years because of its application as a suitable substrate in graphene-based devices [1, 2]. hBN has a hexagonal structure, with van der Waals interactions between layers and only a slight lattice mismatch of less than 2% with graphene [3]. hBN is the most stable and common polytype of boron nitride [4]. Its properties include having a stable structure, ultra-flat surfaces, a wide band gap (6.0 eV) with tunability, a dielectric constant of 2.4, high chemical/thermal stability, and, like many 2D materials it does not have dangling bonds at its surface [5, 6]. The large area deposition of hBN can be achieved using chemical vapour deposition (CVD) amongst other methods [7]. It can be doped as p [8] or n-type [9], with the latter being more challenging. Based on these properties and deposition techniques, hBN has been explored for a variety of applications including dielectrics for transistors to develop ultra-fast low power devices and electronic packaging [6, 10].

A recent application has been the incorporation of hBN in solar photovoltaic cells. For example, hBN has been used as a passivation layer in epitaxial InP-based solar photovoltaic cells [11] with those using hBN monolayers demonstrating an increase in efficiency from 11.5% to 17.2%. The open circuit voltage (V_{oc}), a key metric in solar cells, improved, increasing to 0.8 V with hBN versus 0.72 V without, while the external quantum efficiency (EQE) had a relative increase at shorter wavelengths of ∼20%. Another study also demonstrated improved power conversion efficiencies through the inclusion of hBN in solar cells based on a graphene/hBN/GaAs heterojunction. In that study an increase in efficiency from 8.63% (graphene/GaAs) to 10.18% with the device using the hBN interlayer was reported [12]. In other work, hBN was added into nickel oxide (NiO) hole transport

layers used in p-i-n perovskite solar cells [13]. The motivation was to create a NiO:BN hole transport layer to improve its band alignment with the perovskite layer. Furthermore, the hBN provided better interface contact between the layers due to flatter nature of the NiO:BN as compared to NiO. The result was enhanced charge transportation across the interface and reduced recombination. The efficiencies of the NiO:BN based perovskite solar cells were enhanced by 1.9%, and they demonstrated higher stability over time. hBN was further used as an electron blocking layer in organic solar cells, where the conversion efficiencies of 6.13% and 4.8% for inverted and conventional device structures were attained respectively and performed comparably to devices using conventional hole transport layers [14].

Cadmium telluride (CdTe) is a popular material for commercially available thin-film solar cells owing to its inherent properties (high absorption, direct band gap of ∼1.45 eV) and low-cost manufacturing [15]. While efficiencies have improved, and the short-circuit current of CdTe solar cells is near its limit, the open circuit voltage (0.8759 V) [16] is lower than the potential maximum based on the Shockley Queisser (SQ) limit [17]. For example, GaAs, which has a similar bandgap to CdTe, achieves technological V_{oc} values which are closer to its theoretical SQ limit (V_{oc} = 1.12 V, i.e. 96.5%) than does CdTe which only reaches 75.8% [18]. Various strategies have been investigated to improve the V_{oc} [17, 19], of which one key area has been associated back contact optimisation [17, 20]. An aspect of this is of a hole-selective back contact/electron reflectors to reduce the electron flow from the CdTe layer towards the back surface [21], thereby reducing recombination and improving photoelectron collection. The reflector can be achieved by the inclusion of an additional layer between the solar absorber and the metal contact (e.g. ZnTe [22] or $Cd_{1-x}Mg_xTe$ [23]). There are many requirements for this interface which include, interfacial chemical stability, no deep interface states that could act as recombination centres, good valence band alignment with CdTe reducing barrier for hole transport and high conduction band offset to allow electron reflection at the interface. Another way in which performance can be improved is by introducing an interface which could provide improved passivation. In this study we explored how hBN could be used at the back contact to improve device performance.

To verify the basis of the study, predicted band diagrams for the incorporation of hBN into Sb_2Se_3 and CdTe solar cells were drawn and are shown in figures S1 and S2 respectively. The values such as ionisation potential, band gap used in producing the band diagrams were taken from relevant literature from previous studies. The effective work function of hBN is impacted by both interfacing materials, the metal contact and to a lesser extent the substrate. The effective work function is nearer to that of the metal (Au) hence the rationale for selecting 5.1 eV. Both the solar cells demonstrate a substantial barrier to electrons, with a large conduction band offset of >4 eV in both cases. This would allow the electron blocking/reflection.

At the same time the predicted structure for Sb_2Se_3 provided an approximate valence band barrier of 0.24 eV and ∼0.5 eV for CdTe. In the case of CdTe whilst offset is not negligible, the devices would still be operational. For CdTe solar cells, it has been shown that for valence band barriers from −0.4 eV to +0.3 eV there would be almost no change in efficiency and slight change at −0.5 eV [20]. Also, as explained in [14] where hBN was used in an organic solar cell, a hole barrier of 0.21 eV can still be acceptable given that there is a tunnelling probability through the 2D material. Other studies discuss charge carrier flow through hBN in terms of tunnelling probability. In addition, as set out in the previous studies, other benefits of incorporating 2D hBN include passivation at the interface, which would provide device improvements.

Herein for the first time, we report the fabrication of CdTe and Sb_2Se_3 solar cells that incorporate large-area 2D hBN multilayers at the back contact to act as electron reflectors. The solar cells were fabricated in a superstrate configuration on glass substrates with the solar absorber layers deposited using closed space sublimation (CSS). hBN layers were deposited via CVD and wet-transfer processes. The CdTe solar cells that incorporated hBN, performed better than the controls, achieving an increase in both average and peak performance for efficiency, short-circuit current and open-circuit voltage, with an improvement of 9.9% in the peak efficiency. The Sb_2Se_3 device did not function as a solar cell, and the detailed reasons for this are provided later in section 3.2. This study provides useful insights into the application of 2D hBN in thin-film solar cells.

2. Methods and materials

2.1. 2D hBN growth and deposition

Large area-hBN was deposited in a two-stage process. The first stage was the CVD growth of trilayer hBN on a sapphire wafer (*c*-plane). The hBN growth took place in a low-pressure and plasma enhanced CVD system at 1300 °C. A plasma was generated at 30 W for 30 min in a gas mixture of borazine (0.2 sccm) and Ar (10 sccm) to complete the growth process. The sapphire is a sacrificial substrate, and the second stage entails the wet transfer of the hBN to the solar cell structures. For the wet transfer process a thin film of poly-methyl methacrylate (PMMA) was spin-coated onto the hBN sample to act as a protective layer. The trilayer hBN film was then delaminated via an etching process using diluted hydrofluoric acid (HF). Subsequently hBN and PMMA were transferred onto

the solar cells. The PMMA was then removed by dipping the complete sample into acetone. The solar cell, including the hBN layer, was then completed by the deposition of 50 nm thick Au contacts (99.99%, Goodfellow) formed using a shadow mask.

2.2. CdTe solar cells

The substrates for the solar cells were NSG Ltd TEC^{TM} 15 soda-lime glass, which have a fluorine doped tin oxide (FTO) transparent conductive coating. On top of the substrate a cadmium sulphide (CdS) window layer of 100 nm thickness was deposited using radio frequency (RF) magnetron sputtering with a single CdS target (5 N, Pi-Kem). The sputtering was performed in an AJA International Orion system at power density of 1.32 W cm^{-2} and in 5 mTorr (0.67 Pa) of argon gas, with the substrate held at 200 °C. The CdTe layers were deposited via CSS in custom made equipment (Electro-gas systems, Manchester) using undoped 5 N CdTe (Alfa Aesar) resulting in a thickness of ∼4 μm. To passivate the CdTe grain boundaries and to affect re-crystallisation, a chlorine treatment was applied by spray deposition of aqueous $MgCl_2$ (99+% Alfa Aesar) and subsequent annealing in air at 410 °C in a tube furnace for 20 min. Next, the as-grown CdTe surface was etched in a nitric-phosphoric (NP) solution comprising 70% phosphoric acid, 29% deionized (DI) water, and 1% nitric acid (by volume). The samples were etched for 15 s, rinsed with DI water, and dried with nitrogen gas. The purpose of this etching process is to create a low-resistance back contact [24]. The next step was the deposition of hBN (see earlier). The control devices were fabricated without hBN. Both solar cell types were completed by evaporating the Au contacts (50 nm). The solar cell fabrication procedure has been described elsewhere [25].

2.3. Sb_2Se_3 solar cells

The same NSG Ltd TEC^{TM}15 soda-lime glass substrates were coated with TiO_2 films (∼70 nm) by RF sputtering at 3.3 W cm^{-2} using a TiO_2 target (99.95%, PI-KEM) under 3 mTorr (∼0.4 Pa) of argon gas with 1% O_2 incorporated. This was followed by annealing at 500 °C for 30 min and a 10 min UV/ozone clean. Sb_2Se_3 was then deposited using CSS in two stages: using an initial seed layer and then a growth phase. Further details may be found in [26, 27]. The initial seed layer deposition takes ∼5 min with the source temperature at 350 °C at a pressure of 0.0375 Torr (5 Pa). This was followed by a short annealing stage in N_2 and a second growth stage with the source at 470 °C and ∼10 Torr (1333.22 Pa) for 15 min. The Sb_2Se_3 thickness was ∼2 μm. The next step was hBN deposition which was described earlier and identical for both solar cell types (CdTe and Sb_2Se_3). A control device was also fabricated (without hBN), and the final step was the thermal evaporation of 50 nm gold contacts, as described earlier. During fabrication of the solar cells there was no different thermal annealing that took place between the control solar cells and those using hBN. This was to prevent any other differences apart from the inclusion of the hBN itself.

2.4. Material and device characterisation

For crystallographic analysis a Rigaku SmartLab x-ray diffractometer (XRD) with a rotating 9 kW Cu-Kα source and a Ge (220) 2-bounce monochromator was used. Its 6-axis goniometer with a resolution of 0.001° was used to measure the samples in the out-of-plane geometry. For the identification of the 2D-hBN a HORIBA XploRA^{TM} Raman Microscope was used with the following settings: x50LWD objective lens, 532 nm laser, 1% laser power (0.2 mW), 4 s acquisition, 1 accumulation, 1800 T grating, pinhole aperture of 100 μm in diameter and 100 μm wide slit at the entrance to the spectrograph. For the Raman spectra for the complete solar cell, the equipment, results and settings are mentioned in the supplementary information.

TEM lamella preparation was performed using an FEI Helios G4CX Ga FIB-SEM. For FIB cross sections for SEM examination, the samples were prepared in the following way: 20 nm of iridium (Ir) was sputter coated on the samples initially, followed by 500 nm of platinum (Pt) via electron beam deposition and ∼1 μm of ion beam deposited Pt/C, which is predominately C. The HR-SEM, TEM and energy dispersive x-ray (EDX) spectroscopy analyses of the solar cells were carried out using an FEI Titan3 Themis 300; X-FEG 300 kV S/TEM with S-TWIN objective lens, monochromator (energy spread ∼0.25 eV), multiple HAADF/ADF/BF STEM detectors, and an FEI Super-X 4-detector EDX system.

X-ray Photoelectron Spectroscopy (XPS) was performed to explore surface chemistry. The system consisted of an ultrahigh vacuum system with a base pressure of $<3 \times 10^{-9}$ mbar using a mono-chromated Al Kα source at 1486.6 eV (Omicron XM 1000) and a power of 216 W. XPS measurements were conducted using a spot size of 20 μm. An aperture diameter of 6 mm was used with the sample normal at 45° to both the x-ray source and entrance optics of the hemispherical energy analyser (Omicron EA 125). The XPS spectra were referenced to an adventitious carbon peak at 284.8 eV. Peak deconvolution and fitting were performed manually using the XPSPEAK4.1 software.

The complete solar cells were also characterised. The current density–voltage (J–V) characteristics were measured using a Keithley 2400 source meter and an AAA AM1.5 (1000 W m^{-2}) spectrum delivered from a TS Space Systems solar simulator. EQE measurements were performed using a Bentham PVE300 system.

3. Results and discussion

3.1. Physical materials characterisation

In this section we present characterisation of the materials and structures grown for investigation using SEM, XRD, Raman, TEM and XPS. While the composition of all component layers was as expected, the trilayer hBN was best observed using XPS chemical analysis with further evidence for it coming from the shift in valence band maximum (VBM) from the hBN compared to those of the bare CdTe and Sb_2Se_3 solar cells.

The SEM cross sections showing the configurations of the CdTe and Sb_2Se_3 solar cells are shown in figures 1(a) and (b). The unlabelled layers above the absorbers (CdTe, Sb_2Se_3) comprised the Au contacts and protective layers (Ir, Pt and C) used for the FIB lamellae preparation whereas the hBN layers were not visible at this resolution, given their expected thickness of ∼1 nm (trilayer).

The solar cells were also examined using XRD, and the results for CdTe and Sb_2Se_3 are presented in figures 1(c) and figure S3 respectively. The CdTe device exhibited clear CdTe peaks [28, 29] and a strong (111) preferred orientation. There was also an SnO_2 (200) peak at $\sim 2\theta = 38°$. The CdS layer was not visible in these results. The CdS (102) peak was expected to be observed at 36.70°. The XRD pattern of the (somewhat thinner) Sb_2Se_3 device shown in figure S3 shows many orthorhombic Sb_2Se_3 peaks, together with peaks from the underlying TiO_2 and FTO layers [30]. Interestingly, a detailed examination of the region $26° < 2\theta < 30°$ (figure S4) shows four peaks at $2\theta = 26.48°$, 26.33°, 26.99° and 27.08°. Initially the peak at $2\theta = 26.48°$ was thought to be hBN (002) [31–33]. Upon careful consideration these peaks were found to be due to SnO_2:F (110), which shifted slightly from the SnO_2 reference pattern due to F incorporation. Further hBN peaks associated with (100), (101) and (004) were not observed because the layer was extremely thin.

Raman spectroscopic measurements were performed on both solar cells. The presence of hBN was detected after carefully selecting the settings on the Raman microscope such as low laser power (0.2 mW) and setting the confocal pinhole aperture to 100 μm. Using this configuration the 2D-hBN was consistently observed at 1366.8 cm^{-1} across all samples, which is in line with the fact that these were produced using the same process. Other features of the solar cells were also detected using Raman spectroscopy, with the results and settings provided in the supplementary information (figure S5). In figure S5(a) the Raman spectra for the CdTe solar cell is observed which has peaks at 120 cm^{-1} and 134 cm^{-1} that can be attributed to A1 and E1 phonon vibration modes of Te [34]. The 134 cm^{-1} peak is also related to the transverse optical mode of CdTe. A slight shoulder was observed at ∼160 cm^{-1} which can be associated with the longitudinal optical mode for CdTe [35]. Figure S6b shows the Raman spectrum of the Sb_2Sb_3 solar cell. The peak at approximately 190 cm^{-1} is typically related to Sb–Se vibrations in Sb_2Se_3 [36]. The peak at 250 cm^{-1} is typically related to Sb_2Se_3 however other studies have suggested that it is related to Sb_2O_3 [36, 37]. Three TiO_2 peaks can also be observed in the region of 376 cm^{-1}–629 cm^{-1} [38].

High-resolution TEM images are shown in figures 1(e) and (f) (and Supplementary Information figures S8–S14), which show the key constituents of both devices. Cross sections of the surface regions of both solar cells were examined by TEM in an attempt to observe hBN. These inorganic thin film materials (CdTe, Sb_2Se_3) have a much larger surface roughness than very flat silicon, sapphire and nickel, on which hBN and other 2D materials are typically deposited. For example, CdTe solar cells can have a peak to valley roughness of up to 600 nm [39] and Sb_2Sb_3 can have a roughness of at least 100 nm [40], compared to <0.5 nm for polished silicon. Consequently, it was not possible to visualise hBN in such a way that other publications have shown these layers. The surface SEM images of both solar cells are shown in figures S6 and S7, which confirm the challenging surface morphology of both CdTe and Sb_2Se_3.

The high-angle annular dark-field scanning transmission electron microscopy images in figure 1(e) and f (top-left) show the lighter/brighter Ir coating in the upper half of both images. Careful examination of the STEM image at the interface between Ir and the lower bulk material showed a dark/black stripe. In the case of the CdTe cell the black strip was thinner than that of Sb_2Se_3. This is the region where we expect to observe hBN; therefore, this dark stripe aligns well with the lower atomic numbers associated with hBN in comparison to Ir and CdTe/Sb_2Se_3 layers. Further support for the position of the hBN is the EDX analysis for nitrogen in figures 1(e) and (f). Nitrogen can be seen more clearly in the Sb_2Se_3 image at the interface but is also seen in the CdTe image. It is well known that lighter elements such as boron are much more challenging to observe by EDX owing to the lower energy x-rays generated (<0.5 keV). In addition, the low energy peaks are often masked by the electronic noise of the detector. A further challenge is the large interaction volume of electron beam which can cause the detector to be overwhelmed by signals from the substrate. The EDX spectrum for this image is shown in figure S10(a), where the Cd and Te peaks are present in almost equal proportions and the peaks for the capping layers (C, Pt, and Ir) are clearly visible. It is possible that the presence of carbon can also mask out boron, given that their x-ray peaks would overlap significantly. Light element EDX spectroscopy is a well-known challenge. The EDX spectra of the Sb_2Se_3 device are shown in figure S13. As with the

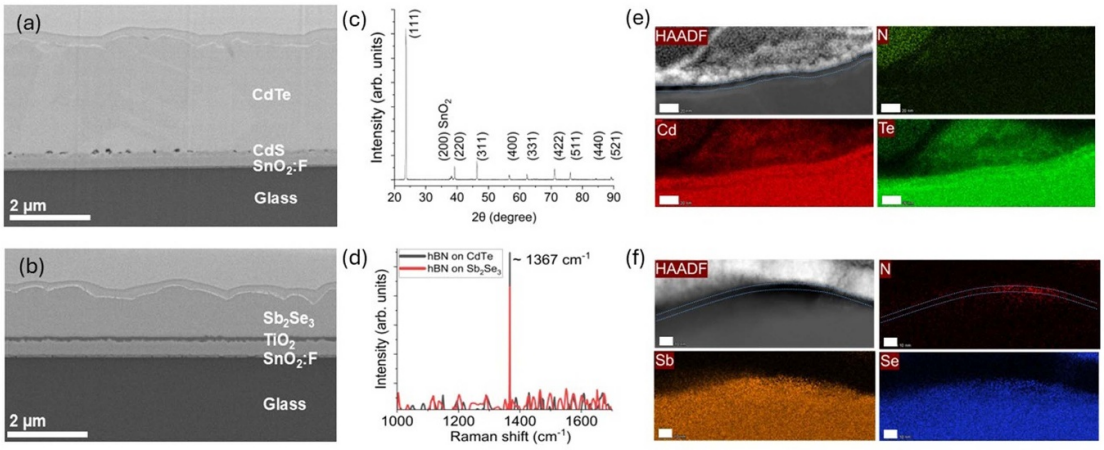

Figure 1. (a, b) HR-SEM cross sections showing the configurations of the glass/FTO/CdS/CdTe and glass/FTO/TiO_2/Sb_2Se_3 solar cells respectively. (The unlabelled layers above the absorbers are Ir/Pt protection layers used in FIB cross-sectioning and hBN is not visible at this resolution). Scale bars: 2 μm (c) X-ray diffractogram of the CdTe solar cell, with only the CdTe crystallographic orientations. (d) Raman spectra of hBN on Sb_2Se_3 and hBN on CdTe (e) HR-TEM of upper surface of CdTe layer solar cell, showing the HAADF image and associated HR-TEM-EDX mapping of N, Cd and Te. Dotted line indicating region for hBN. Scale bar: 20 nm. (f) HR-TEM of upper surface of Sb_2Se_3 solar cell, showing the HAADF image and associated HR-TEM-EDX mapping of N, Sb and Se. Scale bar: 10 nm. Dotted line indicating region for hBN.

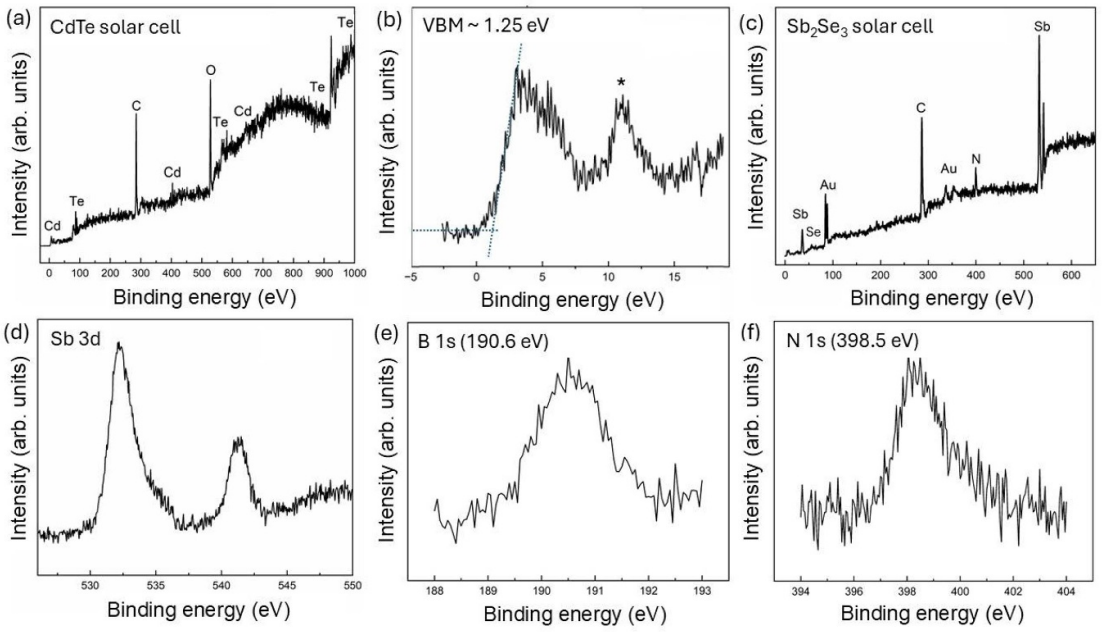

Figure 2. XPS spectra and related results for the two solar cells (a) XPS survey scan for the CdTe solar cell. (b) Valence band maximum (VBM) obtained by XPS for CdTe solar cell (* marks the Cd 4d peak). (c) XPS survey scan for the Sb_2Se_3 solar cell. (d) XPS spectra for the Sb 3d peaks. (e) XPS spectra for the B 1s peak as observed in the Sb_2Se_3 solar cell. (f) XPS spectra for the N 1s peak as observed in the CdTe solar cell.

CdTe device spectra, the main components (Sb, Se, and the capping layer materials) are clearly indicated, but hBN is undetectable.

XPS was used to characterise the CdTe and Sb_2Se_3 solar cells. The broad survey scans for both solar photovoltaic cells are shown in figures 2(a) and (c), with both containing the major element peaks. For example, in the CdTe sample (figure 2(a)) Cd 3d peaks were observed at approximately 404 eV and 412 eV and Te 3d peaks can be seen in the region of 570–580 eV [41]. Other Cd and Te peaks can be seen as well as carbon and oxygen surface contaminants owing to the exposure of the sample to the ambient atmosphere. The N 1s peak is very close to the Cd 3d peak. In addition, the VBM was determined as can be seen in figure 2(b). This shows the VBM at approximately 1.25 eV which is that of the hBN in CdTe solar cell [42, 43].

In the Sb_2Se_3 sample (figure 2(c)), the Sb 4d region is observed at ∼35 eV, which normally

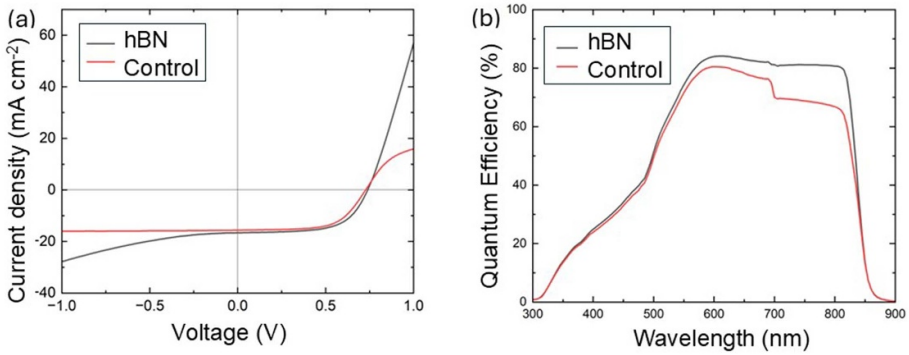

Figure 3. (a) Current–voltage (*JV*) characteristics for the CdTe solar with hBN and without hBN (control sample). (b) External quantum efficiency of both the CdTe solar with hBN and without hBN (control sample).

Table 1. The CdTe solar cells results with hBN monolayers (upper row) and without hBN (lower row). The table displays the best characteristics for efficiency (η), short circuit current (J_{sc}), open circuit voltage (V_{oc}), fill factor (FF), series resistance (R-s) and shunt resistance (R-sh). In brackets the average values (for 12 and 16 devices respectively) as well as the ± standard deviation device parameters (in brackets).

Cell structure	η (%)	J_{sc} (mA cm^{-2})	V_{oc} (V)	FF (%)	*R*-s (Ω)	*R*-sh (Ω)
CdS/CdTe/ h-BN/Au	7.8	16.7	0.74	62.4	12.36	1868.6
	(6.2 ± 3)	(14.9 ± 6.9)	(0.7 ± 0.32)	(59 ± 26.7)	(10.1 ± 4.81)	(748.7 ± 689.0)
CdS/CdTe/Au	7.1	15.9	0.73	62.6	12.00	2907.44
	(3.7 ± 2.4)	(14.4 ± 1.07)	(0.5 ± 0.23)	(45.9 ± 15)	(10.5 ± 1.24)	(257.0 ± 714.3)

indicates Sb_2O_3 and metallic Sb environments [27, 44]. Two Sb 3d peaks at 532 eV and 541 eV are shown in figure 2(e), which are related to both Sb_2Se_3 and Sb_2O_3 [45]. In addition, another Se 3d peak was observed at 54 eV (two peaks merged) as shown in figure 2(d). In the broad scan shown in figure 2(c), the N 1s peak is observed at ∼400 eV.

Detailed XPS scans were undertaken to confirm the precise position and presence of boron and nitrogen as shown in figures 2(e) and 2(f) respectively. Figure 2(e) shows B 1s at 190.6 eV [46] which is characteristic of the B–N bonding signature found in hBN. This peak is not for elemental boron (B–B) which is typically found as a single peak at approximately 187–188 eV [47] or also boron carbide (B–C) observed at ∼188.6 eV [42]. Boron oxide (B_2O_3) is found in the region of 192 eV [43]. Figure 2(f) demonstrates a N 1s peak which is centred around ∼398.5 eV, which is characteristic of nitrogen bonded to boron and very close to other CVD grown hBN layers [48]. If the nitrogen is more oxidised or protonated environments (e.g., amines, ammonium, or nitrates) then this would typically shift further toward 400 eV or higher binding energies. Further, both peaks (1s B and 1s N) are relatively symmetric. The B 1s peak is sharp and matches the ∼1.5 eV FWHM expected for high-quality hBN. Figure S15 shows the VBM obtained via XPS for the Sb_2Se_3 solar cell including the hBN layer at 2 eV.

3.2. Solar cell characterisation

Figure 3(a) shows the *JV* characteristics of CdTe solar cells with and without hBN. For solar cells with hBN layer the improvements in the short circuit current (J_{sc}) and open circuit voltage (V_{oc}) were observed. The 'roll-over' observed in the control solar cell above V_{oc} (i.e. $V > 0.75$ V) is a well-known phenomenon [49], which is due to the formation of a back contact junction diode that opposes the main junction. In the case of hBN this type of roll-over was not observed clearly indicating a change in the back contact potential. In the reverse bias condition at >-0.25 V, the hBN cells deviate from the characteristics of the control solar cell. The EQE (in figure 3(b)) also indicates an improvement in the use of hBN in CdTe solar cells. Improvements can be seen for wavelengths above ∼600 nm, which are associated with reduced recombination losses [50]. The largest improvement in EQE was approximately 15% at 800 nm. The slight feature in the EQE at 700 nm is associated with a switch-over in lamps in the equipment.

Table 1 lists the key solar cell parameters obtained for the CdTe solar cells with and without hBN (control). The table presents both peak values, with the average values presented in brackets (for 12 devices with hBN and 16 without) as well as the standard deviation values. The standard deviation achieved in the control results is comparable to the solar cells results attained in prior projects [51]. These are thin film processes which have variations in film

uniformity, different defects (e.g. pinholes) and varying interface quality resulting in the observed device-to-device differences. From the table we can see that the hBN layer improves the performance of the solar cell across most of the parameters. This improvement was much more apparent in the average values. The average efficiency is improved by 67%, which is principally derived from the improvement in V_{oc}, which on average increased from 0.5 V to 0.7 V. The substantial increase in V_{oc} validates the hypothesis of this approach. The peak series resistance (*R*-s) increases slightly for the hBN based solar cell (12.36 Ω compared to 12.1). The average *R*-s values for the hBN cell were less (10.1 ± 4.81 Ω) than those without hBN (10.5 ± 1.24 Ω), but also showed greater variance. The hBN at the interface between CdTe and the gold contact will certainly affect the series resistance. The greater variance (± 4.81 Ω) may be due to the damage introduced during the hBN transfer process to the solar cell. Controlling the thickness of hBN is also difficult to achieve across larger areas [52]. The average shunt resistance for the hBN-based solar cells was 1.9 times better, indicating the benefit of the hBN layer within the cell reducing recombination and improving the current flow. Figure S16 presents the box and whisker plots of the key device parameters for both the CdTe solar cells using hBN and the control solar cells (CdTe without hBN).

To understand why the Sb_2Se_3 solar cell did not work, it is necessary to review the XPS VBM measurement. That measurement, which included hBN, demonstrated a VBM of 2 eV, which is in effect VBM of the hBN. An XPS measurement without hBN from a previous study using the same fabrication process provided a VBM of 0.91 eV which was the value used in our predicted band diagram. Using the valence band measurement of 2 eV would result in a significantly high valence band offset (>1 eV) which would limit hole current. Another reason for the reduced performance could be due to thicker hBN layer. As we were unable to verify the specific number of hBN layers it could be that in the case of the Sb_2Se_3 device that the hBN was thicker, hence impacting tunnelling.

In a related manner the CdTe solar cell can be explained in terms of the valence band offset also. The measured value for the VBM in this study with hBN on CdTe was approximately 1.25 eV, which is larger than the valence band measurements without hBN of 0.81 eV [51, 53]. The resulting valence band offset in the hBN based CdTe solar cell is approximately 0.44 eV. Whilst this does provide a barrier it is not unsurmountable and the device still operates. Also, this offset needs to be taken in conjunction with the other benefits of that hBN in the CdTe solar cell, which is electron blocking with the substantial conduction band offset and the provision of passivation through the inclusion of hBN.

3.3. Conclusions

In this work we build upon previous studies that have successfully incorporated hBN into single crystal solar cells, with a particular focus on thin-film solar cells. Herein we fabricated CdTe and Sb_2Se_3 solar cells incorporating 2D hBN for the first time. The cells were fabricated in a typical superstrate configuration based on solar absorber layers deposited using CSS. hBN layers were deposited via CVD and wet transfer processes. The solar cells were characterised using a range of techniques including HR-TEM, XRD, Raman spectroscopy and XPS. The CdTe solar cells which incorporated hBN, performed better, achieving an improvement in efficiency, as well as the average V_{oc} improving from 0.5 V to 0.7 V. The EQE was also enhanced by 15% at wavelengths above ∼600 nm. Both the improvement in V_{oc} and enhancement in EQE are indicative of reduced recombination at the back contact, indicating the benefits of including the hBN layer. This was further confirmed by the inoperative Sb_2Se_3 devices. In the case of Sb_2Se_3 it appears that both the electron and hole currents are blocked. This was due to the band misalignment at the back contact. We believe that further studies on the incorporation of 2D hBN into such thin film solar cells could produce an overall benefit to device performance.

Acknowledgments

AM wishes to acknowledge funding from the EPSRC Centre for Doctoral Training in New and Sustainable Photovoltaics (EP/L01551X/1) for this work and the EPSRC SUPERGEN SuperSolar International and Industrial Engagement Fund. We wish to acknowledge the support of the Henry Royce Institute for Advanced Materials through the Researcher Equipment Access Scheme enabling access to the Leeds Electron Microscopy and Spectroscopy Centre (LEMAS) facilities at the University of Leeds; EPSRC Grant Number EP/P022464/1. The authors gratefully acknowledge LEMAS staff for their support and assistance in this work, particularly Dr Zabeada Aslam and John Harrington. We also acknowledge the support of Anna Gilbert, Dr Filipe Braga Nogueira, Professor Laurence Hardwick and Professor Roland Kröger for the Raman measurements.

Data availability statement

All data that support the findings of this study are included within the article (and any supplementary files).

Supplementary Material available at https://doi.org/10.1088/2053-1583/ae8033/data1.

Author contributions

Asim Mumtaz 0000-0002-8982-5206
Conceptualization (lead), Data curation (lead), Formal analysis (lead), Funding acquisition (lead), Investigation (lead), Methodology (lead), Project administration (lead), Resources (supporting), Supervision (supporting), Validation (lead), Visualization (lead), Writing – original draft (lead), Writing – review & editing (lead)

Kyung Yeol Ma 0000-0003-4652-1912
Conceptualization (supporting), Data curation (equal), Investigation (supporting), Methodology (supporting), Project administration (supporting), Writing – review & editing (supporting)

Thomas Shalvey 0000-0002-6008-7561
Data curation (supporting), Formal analysis (equal), Investigation (supporting), Methodology (supporting), Validation (supporting), Visualization (supporting), Writing – review & editing (supporting)

Luke Thomas
Data curation (supporting)

Maha Alotaibi 0000-0002-3887-2854
Data curation (supporting), Formal analysis (supporting), Validation (supporting), Visualization (supporting), Writing – review & editing (supporting)

Gonzalo Vallejo Fernandez 0000-0002-4826-1547
Data curation (supporting), Formal analysis (supporting), Investigation (supporting)

Andrew Pratt 0000-0002-0795-2640
Data curation (supporting), Formal analysis (supporting), Supervision (supporting), Validation (supporting)

Jonathan D Major 0000-0002-5554-1985
Data curation (supporting), Formal analysis (supporting), Investigation (supporting), Project administration (supporting), Resources (supporting), Supervision (supporting), Validation (supporting), Visualization (supporting), Writing – review & editing (supporting)

Hyeon Suk Shin 0000-0003-0495-7443
Conceptualization (supporting), Data curation (supporting), Funding acquisition (supporting), Investigation (supporting), Methodology (supporting), Project administration (supporting), Resources (supporting), Writing – review & editing (supporting)

Ken Durose 0000-0003-1183-3211
Conceptualization (supporting), Data curation (supporting), Formal analysis (supporting), Funding acquisition (supporting), Investigation (supporting), Methodology (supporting), Resources (supporting), Supervision (supporting), Validation (supporting), Visualization (supporting), Writing – original draft (supporting), Writing – review & editing (supporting)

References

[1] Dean C R *et al* 2010 Boron nitride substrates for high-quality graphene electronics *Nat. Nanotechnol.* **5** 722–6
[2] Yankowitz M, Xue J and Leroy B J 2014 Graphene on hexagonal boron nitride *J. Phys.: Condens. Matter.* **30** 303201
[3] Giovannetti G, Khomyakov P A, Brocks G, Kelly P J and van den Brink J 2007 Substrate-induced band gap in graphene on hexagonal boron nitride: ab initio density functional calculations *Phys. Rev. B* **76** 073103
[4] Roy S *et al* 2021 Structure, properties and applications of two-dimensional hexagonal boron nitride *Adv. Mater.* **33** 2101589
[5] Watanabe K, Taniguchi T and Kanda H 2004 Direct-bandgap properties and evidence for ultraviolet lasing of hexagonal boron nitride single crystal *Nat. Mater.* **3** 404–9
[6] Zhang K, Feng Y, Wang F, Yang Z and Wang J 2017 Two dimensional hexagonal boron nitride (2D-hBN): synthesis, properties and applications *J. Mater. Chem.* **5** 11992–2022
[7] Naclerio A E and Kidambi P R 2023 A review of scalable hexagonal boron nitride (h-BN) synthesis for present and future applications *Adv. Mater.* **35** 2207374
[8] Sun F *et al* 2018 P-Type conductivity of hexagonal boron nitride as a dielectrically tunable monolayer: modulation doping with magnesium *Nanoscale* **10** 4361–9
[9] Lu S, Chillón I, Genna V, Vidossich P, Somarowthu S, Pyle A M, De Vivo M and Marcia M 2022 Towards n-type conductivity in hexagonal boron nitride *Nat. Commun.* **13** 1–20
[10] Molaei M J, Younas M and Rezakazemi M 2021 A comprehensive review on recent advances in two-dimensional (2D) hexagonal boron nitride *ACS Appl. Electron. Mater.* **3** 5165–87
[11] Raj V, Chugh D, Black L E, Shehata M M, Li L, Kremer F, Macdonald D H, Tan H H and Jagadish C 2021 Passivation of InP solar cells using large area hexagonal-BN layers *npj 2D Mater. Appl.* **5** 12
[12] Li X, Lin S, Lin X, Xu Z, Wang P, Zhang S, Zhong H, Xu W, Wu Z and Fang W 2016 Graphene/h-BN/GaAs sandwich diode as solar cell and photodetector Opt. Express **24** 134
[13] Mann D S, Patil P, Kim D-H, Kwon S-N and Na S-I 2020 Boron nitride-incorporated NiO_x as a hole transport material for high-performance p-i-n planar perovskite solar cells *J. Power Sources* **477** 228738
[14] Tavakoli M M, Park J-H, Mwaura J, Saravanapavanantham M, Bulović V and Kong J 2021 Monolayer hexagonal boron nitride: an efficient electron blocking layer in organic photovoltaics *Adv. Funct. Mater.* **31** 2101238
[15] Scarpulla M A *et al* 2023 CdTe-based thin film photovoltaics: recent advances, current challenges and future prospects *Sol. Energy Mater. Sol. Cells* **255** 112289
[16] Green M A, Dunlop E, Yoshita M, Kopidakis N, Bothe K, Siefer G, Hao X and Jiang J 2025 Solar cell efficiency tables (version 66) *Prog. Photovoltaics Res. Appl.* **33** 795–810
[17] Hall R S, Lamb D and Irvine S J C 2021 Back contacts materials used in thin film CdTe solar cells—A review *Energy Sci. Eng.* **9** 606–32
[18] Geisthardt R M, Topič M and Sites J R 2015 Status and potential of CdTe solar-cell efficiency *IEEE J. Photovolt.* **5** 1217–21
[19] Sites J and Pan J 2007 Strategies to increase CdTe solar-cell voltage *Thin Solid Films* **515** 6099–102

[20] Gorai P, Krasikov D, Grover S, Xiong G, Metzger W K and Stevanović V, 2023 A search for new back contacts for CdTe solar cells (available at: www.science.org) (https://doi.org/10.1126/sciadv.ade3761)
[21] Hsiao K J and Sites J R, 2009 Electron reflector strategy for CdTe solar cells *IEEE Photovoltaic Specialists Conf.* pp 1846–50
[22] Amin N, Sopian K and Konagai M 2007 Numerical modeling of CdS/CdTe and CdS/CdTe/ZnTe solar cells as a function of CdTe thickness *Sol. Energy Mater. Sol. Cells* **91** 1202–8
[23] Swanson D E, Kobyakov P S, Raguse J, Drayton J, Sites J R and Sampath W S 2014 Reduction of carrier recombination in CdTe solar cells by the addition of a CdMgTe electron reflector Film *40th IEEE PVSC (2014)* (https://doi.org/10.1109/PVSC21196.2014)
[24] Irfan W X, Lin H, Ding H, Tang C W and Gao Y 2012 Nitric-phosphoric acid etching effects on the surface chemical composition of CdTe thin film *Thin Solid Films* **520** 1988–92
[25] Thomas L *et al* 2022 Insights into post-growth doping and proposals for CdTe:In photovoltaic devices *J. Phys. Energy* **4** 045001
[26] Hutter O S, Phillips L J, Durose K and Major J D 2018 6.6% efficient antimony selenide solar cells using grain structure control and an organic contact layer *Sol. Energy Mater. Sol. Cells* **188** 177–81
[27] Shiel H, Hutter O S, Phillips L J, Turkestani M A, Dhanak V R, Veal T D, Durose K and Major J D 2019 Chemical etching of Sb_2Se_3 solar cells: surface chemistry and back contact behaviour *J. Phys. Energy* **1** 045001
[28] Ai X, Yan S, Chen Y, Chen S, Jiang Y, Song X, Ma L and Wu X 2022 Microstructure and optical properties of CdTe thin films prepared by close spaced sublimation method at various growth temperatures *J. Lumin.* **252** 119372
[29] Yimamu A U, Afrassa M A, Dejene B F, Echendu O K, Tshabalala K G, Terblans J J, Swart H C and Motloung S J 2023 Influence of growth time on the properties of CdTe thin films grown by electrodeposition using acetate precursor for solar energy application *Mater. Res. Express* **10** 056403
[30] Don C H *et al* 2024 Reactive DC sputtered TiO_2 electron transport layers for cadmium-free Sb_2Se_3 solar cells *Adv. Energy Mater.* **14** 2401077
[31] Chen X *et al* 2021 Effect of employing chromium as a buffer layer on the crystallinity of hexagonal boron nitride films grown by LPCVD *J. Mater. Sci-Mater El.* **32** 13961–71
[32] Wu P, Lu L, He J, Chen L, Chao Y, He M, Zhu F, Chu X, Li H and Zhu W 2020 Hexagonal boron nitride: a metal-free catalyst for deep oxidative desulfurization of fuel oils *Green Energy Environ.* **5** 166–72
[33] Kim S M *et al* 2015 Synthesis of large-area multilayer hexagonal boron nitride for high material performance *Nat. Commun.* **6** 8662
[34] De Moure-flores F *et al* 2014 CdTe thin films grown by pulsed laser deposition using powder as target: effect of substrate temperature *J. Cryst. Growth* **386** 27–31
[35] Rivera L P *et al* 2019 CdTe:Sn thin films deposited by the simultaneous laser ablation of CdTe and Sn targets *Mater. Res. Express* **7** 015905
[36] Kumar A, Kumar V, Romeo A, Wiemer C and Mariotto G 2021 Raman spectroscopy and *in situ* xrd probing of the thermal decomposition of Sb_2Se_3 thin films *J. Phys. Chem. C* **125** 19858–65
[37] Shongalova A, Correia M R, Vermang B, Cunha J M V, Salomé P M P and Fernandes P A 2018 On the identification of Sb_2Se_3 using Raman scattering *MRS Commun.* **8** 865–70
[38] Balachandran U and Eror N G 1982 Raman spectra of titanium dioxide *J. Solid State Chem.* **42** 276–82
[39] Magginetti D *et al* impact of surface roughness in measuring optoelectronic characteristics of thin-film solar cells *Conf. Record IEEE Photovoltaic Specialists Conf.* Institute of Electrical and Electronics Engineers Inc (https://doi.org/10.1109/PVSC48320.2023.10359832)
[40] Li Z *et al* 2019 9.2%-efficient core-shell structured antimony selenide nanorod array solar cells *Nat. Commun.* **10** 125
[41] Garje S S, Ritch J S, Eisler D J, Afzaal M, O'brien P and Chivers T 2006 Chemical vapour deposition of II–VI semiconductor thin films using $M[(TeP^iPr_2)_2N]_2$ (M=Cd, Hg) as single-source precursors *J. Mater. Chem.* **16** 966–9
[42] Jacobsohn L G, Schulze R K, Maia da Costa M E H and Nastasi M A 2004 x-ray photoelectron spectroscopy investigation of boron carbide films deposited by sputtering *Surf. Sci.* **572** 418–24
[43] Pilli A, Jones J, Chugh N, Kelber J, Pasquale F and LaVoie A 2019 Atomic layer deposition of BN as a novel capping barrier for B_2O_3 *J. Vac. Sci. Technol. A* **37** 041505
[44] Jain A K, Gopalakrishnan C and Malar P 2022 Study of pulsed laser deposited antimony selenide thin films *J. Mater. Sci-Mater El.* **33** 10430–8
[45] Shiel H *et al* 2020 Natural band alignments and band offsets of Sb_2Se_3 solar cells *ACS Appl. Energy Mater.* **3** 11617–26
[46] Ma C, Park J, Liu L, Kim Y-S, Yoon M, Baddorf A P, Gu G and Li A-P 2016 Interplay between intercalated oxygen superstructures and monolayer h-BN on Cu(100) *Phys. Rev. B* **94** 064106
[47] Ong C W, Huang H, Zheng B, Kwok R W M, Hui Y Y and Lau W M 2004 x-ray photoemission spectroscopy of nonmetallic materials: electronic structures of boron and BxOy *J. Appl. Phys.* **95** 3527–34
[48] Zhu Z, Zhang Z, Wang S, Zou J, Gan Y, Yang R, Zhang Y and Long B 2023 Hexagonal boron nitride thick film grown on a sapphire substrate via low-pressure chemical vapor deposition *Cryst. Growth Des.* **23** 7662–8
[49] Zhou J *et al* 2007 The mechanism of J-V 'roll-over' in CdS/CdTe devices *Materials Research Society Symp. Proc.* (Materials Research Society) pp 491–6
[50] Bothwell A M, Drayton J A, Jundt P M and Sites J R 2019 Characterization of thin CdTe solar cells with a CdSeTe front layer *MRS Adv.* **4** 2053–62
[51] Major J, Phillips L, Al Turkestani M, Bowen L, Whittles T, Dhanak V and Durose K 2017 P3HT as a pinhole blocking back contact for CdTe thin film solar cells *Sol. Energy Mater. Sol. Cells.* **172** 1–10
[52] Ma K Y, Kim M and Shin H S 2022 Large-area hexagonal boron nitride layers by chemical vapor deposition: growth and applications for substrates, encapsulation, and membranes *Acc. Mater. Res* **3** 748–60
[53] Kuciauskas D, Perkins C L, Nardone M, Lee C, Mallick R and Xiong G 2023 Band bending at CdTe solar cell contacts: correlating electro-optical and X-ray photoelectron spectroscopy analyses of thin film solar cells *Solar RRL* **7**